

A Pore-Scale Investigation of the Transient Response of Forced Convection in Porous Media to Inlet Ramp Inputs

Rabeeah Habib¹

James Watt School of Engineering,
University of Glasgow,
Glasgow G12 8QQ, UK
e-mail: r.habib.1@research.gla.ac.uk

Bijan Yadollahi

James Watt School of Engineering,
University of Glasgow,
Glasgow G12 8QQ, UK
e-mail: byadollahi@cmclinnovations.com

Nader Karimi

James Watt School of Engineering,
University of Glasgow,
Glasgow G12 8QQ, UK;
School of Engineering and Materials Science,
Queen Mary University of London,
London E1 4NS, UK
e-mail: karimi.melb@gmail.com

This paper investigates the transient response of forced convection of heat in a reticulated porous medium through taking a pore-scale approach. The thermal system is subject to a ramp disturbance superimposed on the entrance flow temperature/velocity. The developed model consisted of ten cylindrical obstacles aligned in a staggered arrangement with set isothermal boundary conditions. A few types of fluids, along with different values of porosity and Reynolds number, are considered. Assuming a laminar flow, the unsteady Navier Stokes and energy equations are solved numerically. The temporally developing flow and temperature fields as well as the surface-averaged Nusselt numbers are used to explore the transient response of the system. Also, a response lag ratio (RLR) is defined to further characterize the transient response of the system. The results reveal that an increase in amplitude increases the RLR. Nonetheless, an increase in ramp duration decreases the RLR, particularly for high-density fluids. Interestingly, it is found that the Reynolds number has almost negligible effects upon RLR. This study clearly reflects the importance of conducting pore-scale analyses for understanding the transient response of heat convection in porous media. [DOI: 10.1115/1.4047968]

Keywords: unsteady forced convection, porous media, transient response, pore-scale analysis, ramp input, heat energy generation/storage/transfer

1 Introduction

Comprehending the transient response of porous media has grown in importance with its widespread use in emerging technologies [1–5]. Cases can be found in the use of heat exchangers [6], micro chemical reactors [7–9], fuel cells [10,11], and electrochemical systems [12,13]. Understanding the response of these systems is vital as the inlet fluid flowrate can be highly time-dependent [14]. It is fundamental to have the ability to predict the thermal response of the pertinent model subject to time-dependent disturbances at the inlet [15]. Steady flow has been the predominant focus of majority of existing studies of forced convection in porous media. This pattern is clearly visible in numerical investigations that were conducted using a pore-scale approach (e.g., Refs. [16–18]) and especially in those studies that took a macroscopic modeling approach (e.g., Refs. [19–22]).

A smaller amount of macroscopic investigations have analyzed unsteady and pulsating flows in porous media as will be discussed in the core part of this literature review. Fewer studies reported results using the pore-scale approach, with most studies being in the two-dimensional domain [8,13,23,24] and even less in the three-dimensional domain [9,25]. In order to fully comprehend steady and unsteady macroscopic modeling, a brief examination of literature on macroscopic studies in porous media is carried out using the Darcy model and its extensions. It is generally understood that a macroscopic model might be lacking for the analysis of periodic flow systems [12]; therefore, a pore-scale approach is employed in this paper.

Saito and de Lemos [26] proposed two-macroscopic-energy equation models for conduction and convection for packed beds of porous media assuming local thermal non-equilibrium. The authors

modeled a two-dimensional unit cell model with square cylinders in a staggered arrangement, replicating Kuwahara et al.'s [27] physical model. Saito and de Lemos [26] numerically solved for the interfacial heat transfer coefficient, discretizing the macroscopic governing equations using the control volume method. The authors of Ref. [26] found their work to be in agreement with Kuwahara et al. [27]. They concluded that a higher porosity medium could reduce the energy transfer between the solid and fluid phase [26]. Lu et al. [28] simulated temperature disturbances during the mixing process of a T-junction filled with and without porous media. They implemented local thermal equilibrium model and concluded that the addition of porous media within the T-junction model lowers the temperature fluctuations during the mixing process [28].

Kim et al. [29] numerically simulated a two-dimensional channel filled with porous media to investigate the effects of forced oscillatory flow on the Nusselt number. Isothermal boundary conditions were set to the channel walls where the porosity of the porous media was fixed to 0.6. The authors of Ref. [29] compared the temperature and flow fields with ranges of pertinent parameters and discovered oscillatory flow to reduce heat transfer in the entrance region of the model when compared to steady flow. They further reported enhanced heat transfer in the central region of the model. A similar study was conducted by Guo et al. [30] who considered the effects of pulsating flow on heat transfer in a pipe partially filled with porous media. The system was modeled as two-dimensional with porous media attached to the walls of the pipe. Guo et al. [30] found that the Nusselt number monotonically increases with the growth in the porous layer thickness.

Bhargava et al. [31] present finite element solutions for a non-Newtonian fluid experiencing pulsation. The analysis was conducted by adopting a one-dimensional transient model depicting a porous medium conduit. The pulsatile effects of the pressure gradient on the model flow were examined by altering parameters such as Reynolds number, pulsating amplitude, and frequency. Bhargava et al. [31] discovered the velocity to augment with an increase in permeability and a reduction of non-Newtonian behavior. Huang and Yang [32] studied forced oscillatory convection in a parallel plate

¹Corresponding author.

Contributed by the Advanced Energy Systems Division of ASME for publication in the JOURNAL OF ENERGY RESOURCES TECHNOLOGY. Manuscript received May 8, 2020; final manuscript received June 8, 2020; published online August 21, 2020. Assoc. Editor: Larry K. B. Li.

channel with porous blocks mounted to the lower wall. They described the effects of varying the amplitude, frequency, and porous blockage ratio on the flow field and heat transfer of the model. An oscillatory flow was introduced to improve flow mixing and greater thermal transport, revealing that heat transfer augments from the heat sources with the rise of the oscillation amplitude.

A numerical study was conducted by Dhahri et al. [33] to find the effects of pulsating flow on entropy generation within a pipe partially filled with porous media. The authors monitored the response of the amplitude, frequency, porous layer thickness, and thermal conductivity ratio with respect to entropy generation. They discovered the temperature difference in the fluid region to be greater than that of the porous region. Farooghi et al. [34] studied steady and oscillating flow in a parallel plate channel partially composed with porous media in the upper and lower walls of the channel, subjecting to a constant heat flux. The authors employed the Brinkman-Forchheimer-extended Darcy model and implemented the local thermal non-equilibrium (LTNE) method and reported that local thermal equilibrium (LTE) method overestimates the heat transfer. Farooghi et al. [34] suggested that augmenting the amplitude of flow oscillation could result in an increase in the time-averaged Nusselt number. They further noted the thermal conductivity ratio to increase heat transfer between the solid and the fluid, if the porous media thickness is kept constant.

Ghafarian et al. [35] computed pulsating flow through a channel filled with a porous medium to analyze the heat transfer. Various studies were conducted by altering the frequency, amplitude, and Reynolds number of the working fluid as well as a change of porosity. The local Nusselt number was calculated for a laminar model to monitor heat transfer, showing that the Nusselt number to augment with the use of a high amplitude and high frequency. Targui and Kahalerras [6] numerically simulated oscillatory flow through a double pipe heat exchanger coupled with porous baffles. It was found that the oscillation has a profound effect on heat transfer and maximizes it when only the hot fluid flow oscillates. Zaman et al. [36] numerically examined the flow of blood induced with pulsatile flow within a porous-saturated overlapping stenosed artery. The study depicted a pathological solution where the blood travels through an artery comprising of blood clots and fatty cholesterol. The numerical simulation showed the effects of flowrate, velocity, and wall shear stress on the porous medium. It was found that with a larger permeability the resistance of the flow is smaller whilst the flowrate and velocity augment.

It is observed that the existing studies on unsteady forced convection are mostly concerned with the macroscopic analysis by using the extended Darcy models. Further, most studies include two-dimensional simulations and gave little attention to the transient response of the system. Therefore, there is currently a gap in understanding the thermal transient response at pore scale in a three-dimensional domain. The current investigation aims to address this issue.

2 Methodology

2.1 Problem Configuration, Governing Equations, and Assumptions. In the current pore-scale model, the flow is assumed to be unsteady and laminar. The mass, momentum, and energy conservations [37] for such flow are written as follows.

$$\begin{aligned} \frac{\partial \rho}{\partial t} + \frac{\partial(\rho u_x)}{\partial x} + \frac{\partial(\rho u_y)}{\partial y} + \frac{\partial(\rho u_z)}{\partial z} &= 0 \quad (1) \\ \rho \left(\frac{\partial u_x}{\partial t} + u_x \frac{\partial u_x}{\partial x} + u_y \frac{\partial u_x}{\partial y} + u_z \frac{\partial u_x}{\partial z} \right) & \\ = -\frac{\partial p}{\partial x} - \frac{\partial}{\partial x} \left[-2\mu \frac{\partial u_x}{\partial x} + \frac{2}{3}\mu \left(\frac{\partial u_x}{\partial x} + \frac{\partial u_y}{\partial y} + \frac{\partial u_z}{\partial z} \right) \right] & \\ - \frac{\partial}{\partial y} \left[-\mu \left(\frac{\partial u_x}{\partial y} + \frac{\partial u_y}{\partial x} \right) \right] - \frac{\partial}{\partial z} \left[-\mu \left(\frac{\partial u_x}{\partial z} + \frac{\partial u_z}{\partial x} \right) \right] & \quad (2a) \end{aligned}$$

$$\begin{aligned} \rho \left(\frac{\partial u_y}{\partial t} + u_x \frac{\partial u_y}{\partial x} + u_y \frac{\partial u_y}{\partial y} + u_z \frac{\partial u_y}{\partial z} \right) & \\ = -\frac{\partial p}{\partial y} - \frac{\partial}{\partial x} \left[-\mu \left(\frac{\partial u_x}{\partial y} + \frac{\partial u_y}{\partial x} \right) \right] & \\ - \frac{\partial}{\partial y} \left[-2\mu \frac{\partial u_y}{\partial y} + \frac{2}{3}\mu \left(\frac{\partial u_x}{\partial x} + \frac{\partial u_y}{\partial y} + \frac{\partial u_z}{\partial z} \right) \right] & \\ - \frac{\partial}{\partial z} \left[-\mu \left(\frac{\partial u_y}{\partial z} + \frac{\partial u_z}{\partial y} \right) \right] & \quad (2b) \end{aligned}$$

$$\begin{aligned} \rho \left(\frac{\partial u_z}{\partial t} + u_x \frac{\partial u_z}{\partial x} + u_y \frac{\partial u_z}{\partial y} + u_z \frac{\partial u_z}{\partial z} \right) & \\ = -\frac{\partial p}{\partial z} - \frac{\partial}{\partial x} \left[-\mu \left(\frac{\partial u_x}{\partial z} + \frac{\partial u_z}{\partial x} \right) \right] & \\ - \frac{\partial}{\partial y} \left[-\mu \left(\frac{\partial u_y}{\partial z} + \frac{\partial u_z}{\partial y} \right) \right] & \\ - \frac{\partial}{\partial z} \left[-2\mu \frac{\partial u_z}{\partial z} + \frac{2}{3}\mu \left(\frac{\partial u_x}{\partial x} + \frac{\partial u_y}{\partial y} + \frac{\partial u_z}{\partial z} \right) \right] & \quad (2c) \end{aligned}$$

$$\rho c_p \left(\frac{\partial T}{\partial t} + \frac{\partial u_x T}{\partial x} + \frac{\partial u_y T}{\partial y} + \frac{\partial u_z T}{\partial z} \right) = k_f \left(\frac{\partial^2 T}{\partial x^2} + \frac{\partial^2 T}{\partial y^2} + \frac{\partial^2 T}{\partial z^2} \right), \quad (3)$$

where all terms have been defined in the Nomenclature.

A representative elementary volume (REV) similar to the structure used in Ref. [17] is taken into consideration. The REV contains a single pore around an obstacle [38]. Such a unit is periodically repeated in each direction to create the large-scale porous structure. Therefore, it is safe to assume nearly identical flows in each REV unit. As a result, the boundaries of this unit element are treated as periodic and symmetric.

The first set of investigations incorporated the REV as a separate unit. The porosity of the unit could be regulated by changing the pore dimensions as obstacle dimensions. In this instance, the pore was selected to be of $0.1 \times 0.2 \text{ m}^2$ and a circular obstacle of diameter 0.05 m was designed in the domain. The flow was assumed to be in steady-state. All solid walls were set to a constant temperature of 300 K with no slip boundary conditions. The fluid properties were established to be standard air. Uniform velocity boundary conditions are applied at the inlet, and the temperature was set to 200 K and atmospheric pressure at the outlet. Top and bottom of the pore were treated as symmetry boundaries. Periodic boundary conditions were set at the inlet and outlet for another batch of simulations. All other settings were kept the same as the previous investigations. This replicated the unit structure for the porous media model based on the approach obtained by Saito and de Lemos [21]. It should be devised, however, that while this model is near-identical depiction of the internal structure in a porous medium, it is restricted to steady-state conditions. Consequently, it was decided to follow a systematic approach to produce a representative model which could be employed for unsteady simulations. The rudimentary steady-state REV unit model was devised as a foundation model, with velocity entrance and pressure exit boundaries. In this instance, a script was created where the velocity, as well as the temperature profiles were re-inserted from the exit to the entrance of the model [39]. Therefore, the simulation continued till the variance amongst the inlet and outlet fell beneath a certain value, defined as relative profile change (RPC) as below:

$$\text{RPC} = \left(\sum_{\text{profile}} \frac{|\psi_{\text{outlet}} - \psi_{\text{inlet}}|}{\psi_{\text{outlet}}} \right) \cdot 100 \quad (4)$$

where ψ is either velocity or temperature. The RPC is collated upon every position on the boundary as a percentage unit. The effects of three Reynolds numbers were tested in this part of the study. The outcomes of the investigation have been depicted in Fig. 1. It is clear that the difference in profiles falls below 5% after nine

iterations for all three Reynolds numbers. After this, the profiles remain almost the same. Thus, it was settled that the representative model could be produced using a terrain made up of ten REV's (see Fig. 2). The terrain geometry was then verified at identical conditions as the periodic model showing that the temperature and pressure profiles at the outlet almost match with those profiles after nine levels of insertion. Further, with the use of periodic boundary conditions, the results were found to be almost identical. This confirmed the proper construction of the computational model used in the rest of the current study.

A series of steady-state investigations were performed on the terrain model to study the effects of main variables affecting the fluid flow inside the system. Three porosities of 0.87, 0.8, and 0.72 were considered. Uniform velocity and 300 K constant temperature were set at the inlet and atmospheric pressure was set at the outlet. Three wall temperatures of 500, 600, and 700 K were also tested with 300 K inlet temperature. The effects of circular obstacle geometries were investigated, and the Nusselt number was calculated separately on each obstacle to enable a more detailed evaluation of the results.

Under unsteady condition, a ramp-up was selected as the method for temporal variations as one of the most common scenarios in real applications. The inlet flow was modulated by superimposing a ramp-up on the inlet velocity after 5 s. That is,

$$u(0, t) = u_{in} \cdot \left(1 + \frac{t}{t_{ramp} \cdot a} \right) \quad (5)$$

The Reynolds number [40] was defined by the following relation:

$$Re_L = \frac{u_{in} \rho D}{\mu} \quad (6)$$

Newton's law of cooling [37] is expressed as

$$q_f'' = h_o(T_f - T_{ref}) \quad (7)$$

The Nusselt number is surface-averaged for all obstacles to assess the thermal response of the pore-scale model. The following equation is employed to calculate the Nusselt Number [41]

$$Nu_L = \frac{q_f'' D}{k_f(T_f - T_{ref})} \quad (8)$$

Along with the aforementioned Re and porosity values, three ramp durations of 10, 20, and 30 s were investigated along with three ramp-up levels of 10, 20, and 30% of the base value. All the investigations were tested for ramp-ups in inlet temperature

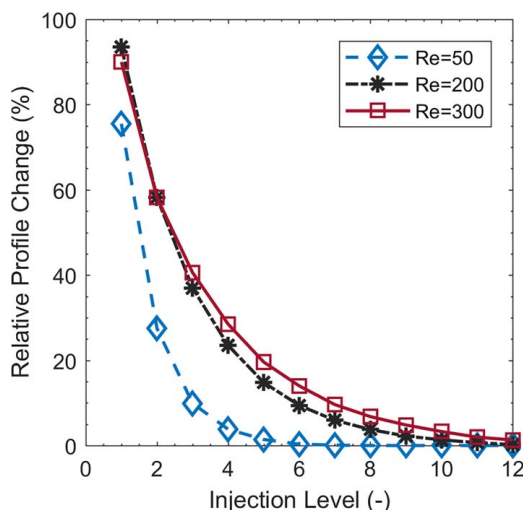


Fig. 1 Accumulative relative profile change versus re-injection iteration at different Reynolds numbers

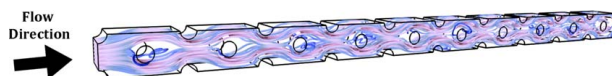


Fig. 2 A three-dimensional view of the terrain model used for unsteady investigations visualizing fluid flow

and velocity. Furthermore, three fluids as air, CO₂, and H₂ were tested. A total of around 500 different settings were investigated in the course of this investigation.

2.2 Numerical Methods

2.2.1 Computational Techniques. A numerical model was developed using the commercial software STAR-CCM+. A satisfactory refined mesh of polyhedral cells was formed for the bulk region (Fig. 3(a)). In total, 15 high-quality, tetrahedral, or “prism layer” cells were generated per solid surface to ensure higher accuracy of gradient calculations. All equations were solved using a second-order discretization technique where a coupled solver was implemented for greater stability. The boundary conditions were set according to each case as described in Sec. 2.1. Stagnant flow along with ambient pressure and temperature were set as the initial conditions for all cases except for the unsteady simulations. For these cases, the converged solution from similar steady-state simulation was used instead. The central time-step chosen was that in which the magnitude was lesser by a factor of 100 in comparison with that of the physical timescale. In order to reduce the runtime of ramp cases, a variable time-step approach was adopted. These time-steps were refined around the ramp section for more accuracy.

A minimum magnitude of 10⁻⁶ for all equations residual levels were achieved for all steady-state simulations. Furthermore, a sizeable parameter was selected for upper limit time-step number in ramp cases, and mean temperature at the exit was analyzed to monitor convergence with respect to time. A new stoppage criterion was defined to terminate the simulations if the deviation in the last 1000 time-steps is lower than 0.5 K [42]. These proved to be adequate convergence criteria for almost all cases.

2.2.2 Grid Independency and Validation. Surface-averaged Nusselt numbers were calculated individually for each obstacle. Although these values are a single measure for steady-state

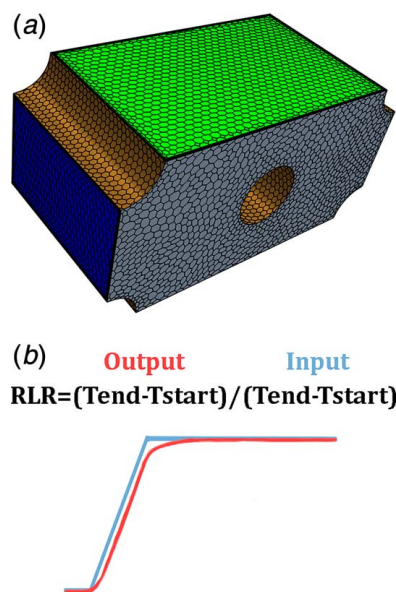


Fig. 3 (a) Single-pore structural unit as implemented in the current simulations and (b) schematic representation for the definition of RLR

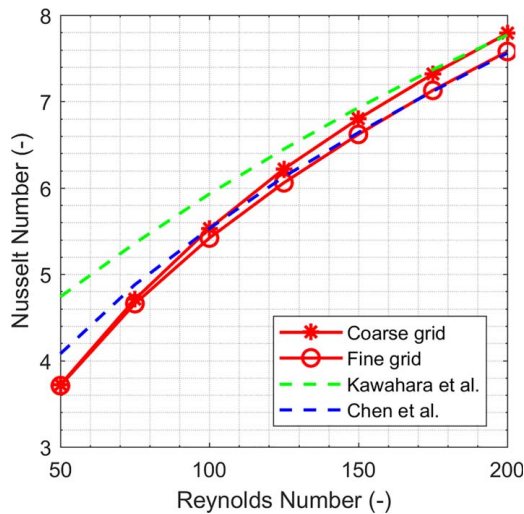


Fig. 4 A comparison of Nusselt Number values in heat transfer validation case

simulations, a temporal variations plot was produced for unsteady simulations. Steady-state results were normalized with their final settled value on each pore. Temporal variations in either velocity or temperature were introduced at the entrance of the model. System response was checked via the Nusselt number over obstacles. Ideally, the same variation profile should convect to each obstacle at a speed of bulk velocity. However, this is not the case in real flows because of the lags incorporated by the viscous flow. A lag could be introduced as the flow-induced elongation in the ramp section, designated as RLR

$$\text{RLR} = \frac{(t_{\text{end}} - t_{\text{start}})_{\text{output}}}{(t_{\text{end}} - t_{\text{start}})_{\text{input}}} \quad (9)$$

RLR is a non-dimensional quantity, calculated for the Nusselt number response of each obstacle. A graphical representation for the RLR definition is shown in Fig. 3(b).

Figure 4 shows the validation case performed on Nusselt number predictions. Two separate studies of Chen and Wung [43] and Kawahara et al. [27] were selected. A correlation for heat transfer in structures similar to those of the current study has been proposed in each of these studies. These correlations are based on experimental and numerical data defined by

$$\overline{\text{Nu}} = 0.78\text{Re}^{0.45}\text{Pr}^{0.38} \quad (10)$$

$$\text{Nu} = \left(1 + \frac{4(1 + \varepsilon)}{\varepsilon}\right) + \frac{1}{2}(1 + \varepsilon)^{1/2}\text{Re}^{0.6}\text{Pr}^{1/3} \quad (11)$$

Equation (10) was derived to represent a staggered arrangement whereas Eq. (11) was extracted particularly for square obstacles. Both correlations can be used for a large range of properties and Reynolds numbers. The close similarity of the simulated results

and the correlations confirms the validity of the numerical simulations.

The computational mesh was systematically refined to find the ideal balance between the relative accuracy and low computational costs. A total of seven grids were created between a range of 2600–2,570,000 cells. Early investigations on a single Reynolds number showed that the Nusselt number shows minimal variance for grid ranges between 225,000–2,570,000 cells. However, further refinement in the grid sizes did not show any significant change in the results (as shown in Fig. 4). Therefore, it is safe to argue that the results are grid independent using the 613,000 cell grid.

3 Results and Discussion

Figure 5 illustrates the spatial response of the ten obstacles pore-scale model to a steady inlet flow velocity. This figure displays snapshots of three configurations where the wall temperature alters at intervals of a 100 K for their respective converged solutions. The inlet flow enters at ambient temperature from the left-hand side and exits toward the right. As the inlet flow travels downstream, the constant temperature around the circular obstacles influences the flow field around and behind the obstacles, creating wake regions. This effect is readily observed in the flow field where there is a larger temperature difference between the inlet flow and the circular obstacles and is particularly visible when the wall temperature is at its lowest. Such effects decay after the third obstacle as the flow travels downstream almost appearing to have reached thermal equilibrium. However, the diffusion effects are the strongest throughout the porous configuration when the obstacle temperature is the largest. This can be seen when the wall temperature is 700 K, and the flow field appears to reach very close to thermal equilibrium further downstream at the tenth obstacle. The flow field behavior and temperature change is monitored throughout the system by the surface-averaged Nusselt Number around each circular obstacle. The analyses discussed in this section aim to understand the transient response by observing the response lag ratio (RLR) of the pore-scale model subject to an unsteady ramp input.

A comparison of Nusselt numbers is made for the inlet flow subject to a ramp between inlet temperature and inlet velocity in Fig. 6(a). As the velocity ramp is introduced, the first obstacle responds gradually albeit the largest increase in the Nusselt number is also reported. The opposite is observed at obstacles closer to the outlet with quicker response time and lesser augmentation in the Nusselt number. This is expected to be due to the thermal boundary conditions set for the circular obstacles. As the time-dependent ramp travels throughout the model, the viscous effects continue to decay with the rate of heat transfer plummeting as it reaches the outlet. A similar trend is observed when the system is subject to an inlet temperature ramp. To achieve constant convective heat transfer, the system requires less time when the flow is closer to the outlet when compared to the inlet. As the inlet temperature rises, the local temperature difference between the fluid and solid surfaces decreases. This limits the rate of heat transfer and reduces the Nusselt number when compared with the steady-state value. It is noteworthy that the heat transfer rate per obstacle and response time both change when the system is subject to a velocity ramp whereas only response time differs when the system is subject to a temperature ramp. Figure 6(b) displays the response lag ratio

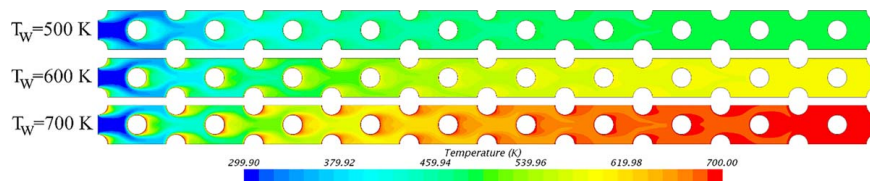


Fig. 5 The effect of wall thermal boundary conditions on steady temperature fields, fluid type: H₂, $\varepsilon = 0.804$, and $\text{Re} = 250$

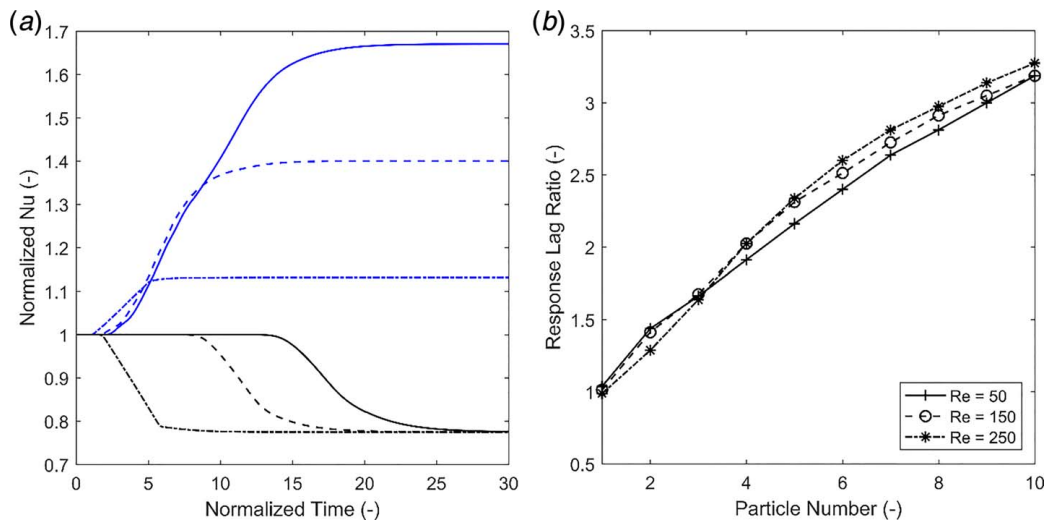


Fig. 6 (a) A comparison between normalized Nu results for ramp in velocity (blue) and temperature (black) on first (solid), sixth (dash) and tenth (dash-dot) pores, fluid type: CO₂, $\varepsilon = 0.874$, $Re_L = 150$, $R = 30$ s, and $a = 30\%$. **(b)** The effect of Reynolds number on RLR, fluid type: H₂ at $\varepsilon = 0.804$, $R = 20$ s, and $a = 20\%$. (Color version online.)

for each obstacle. The lag augments as the fluid travels downstream of the model where the viscous effects resist the inertial forces of the fluid flow. As the Reynolds number increases, the viscous effects are also amplified, inflating the overall lag of the system. This phenomenon is further analyzed in Fig. 7, visualizing the spatiotemporal flow field snapshots equally split over the respective ramp duration. The time-dependent inlet temperature is subject to an increase of 30% of its base value. In Fig. 7(a), it can be seen before the introduction of the ramp, and the flow field of the obstacles closer to the exit of the system exhibits higher temperature readings, almost matching the temperature of the surface of the obstacles (700 K). As the inlet ramp in temperature is introduced, the overall flow field temperature surges, forcing the higher temperatures to move further upstream. This is because the convective heat transfer diminishes as the gap between the temperature difference narrows, decreasing the Nusselt number.

However, the opposite is observed in Fig. 8 where the temporal evolutions for the velocity field are introduced by a 10-s ramp input. Thus, the increase in velocity and constant temperature at the circular obstacles provide a streamlined contour pattern where convective heat transfer is increasing. Also, as the Reynolds number increases further with the ramp so does the inertial effects of the flow, combined with the thermal diffusion occurring at the circular obstacles, the wake region expands gradually with the

passage of time. It is apparent from Fig. 8 that there is a greater wake flow when compared to Fig. 9, which is lower in the Reynolds number. This can also be observed between Figs. 9(a) and 9(e) where the wake flow contours surge in velocity as the Reynolds number augments. A similar pattern is also observed in the general flow between the two configurations, where a more streamlined contour pattern is observed as the flow moves toward the outlet for a high Reynolds number and a more scattered wider flow pattern for the lower Reynolds number.

An identical configuration to Fig. 8 is presented in Fig. 10 where the working fluid has been switched from air to hydrogen. A similar streamlined contour flow field is observed to that of air; however, there is a drastic increase in the system's velocity albeit the same Reynolds number. This is primarily due to the fluid properties. Hydrogen inhibits a lower density than air, making the fluid lighter therefore more responsive to the identical Reynolds number. This trend is clearly observed during the general flow of the model and within the wake region as the ramp input is implemented. It is understood for a high-density working fluid with identical configuration in the pore-scale model, and the system will exhibit a lower fluid velocity, therefore making it less sensitive to inlet disturbances in comparison with a low-density fluid.

Although the fluid properties of hydrogen make it more sensitive to inlet disturbances, it also appears to be a lot more responsive to

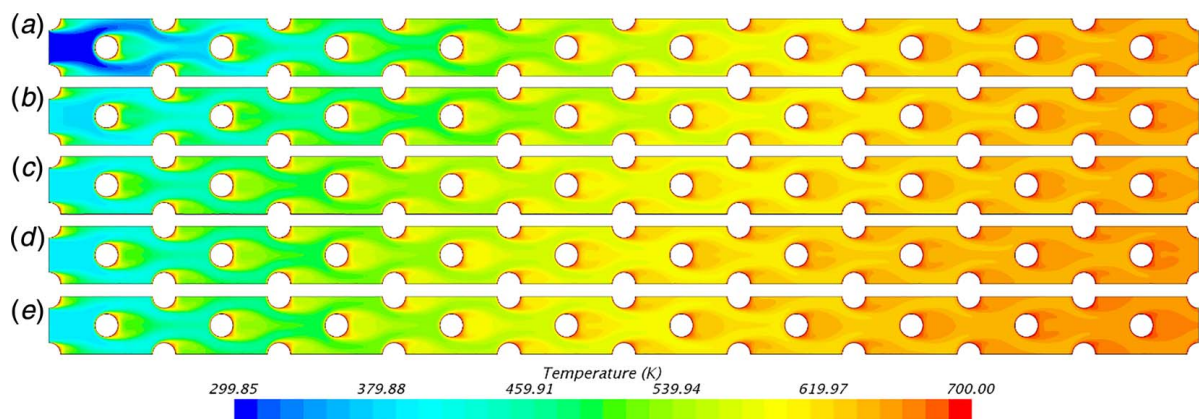


Fig. 7 Temporal evolution of the temperature field with 10-s ramp duration (on temperature) for air at $Re = 250$, $\varepsilon = 0.874$

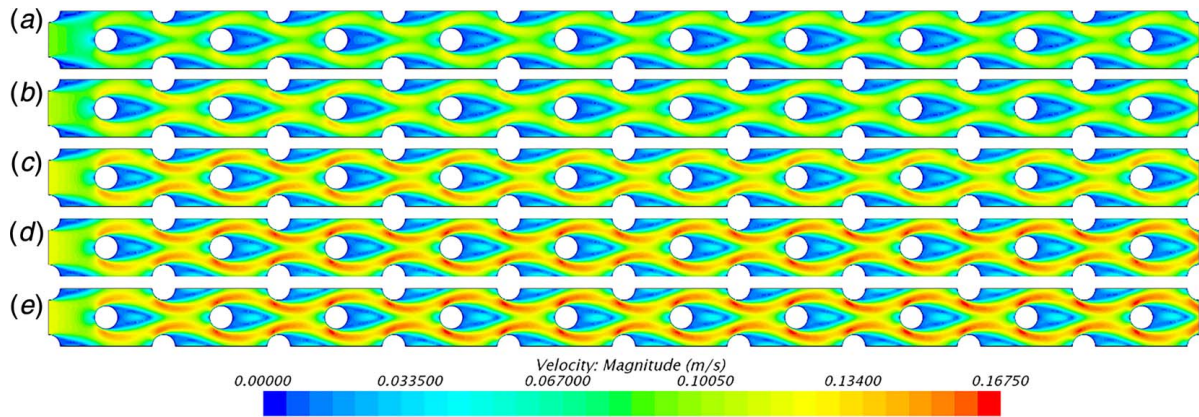


Fig. 8 Temporal evolution of the velocity field with 10-s ramp duration (on velocity) for air at $Re = 250$, $\varepsilon = 0.874$

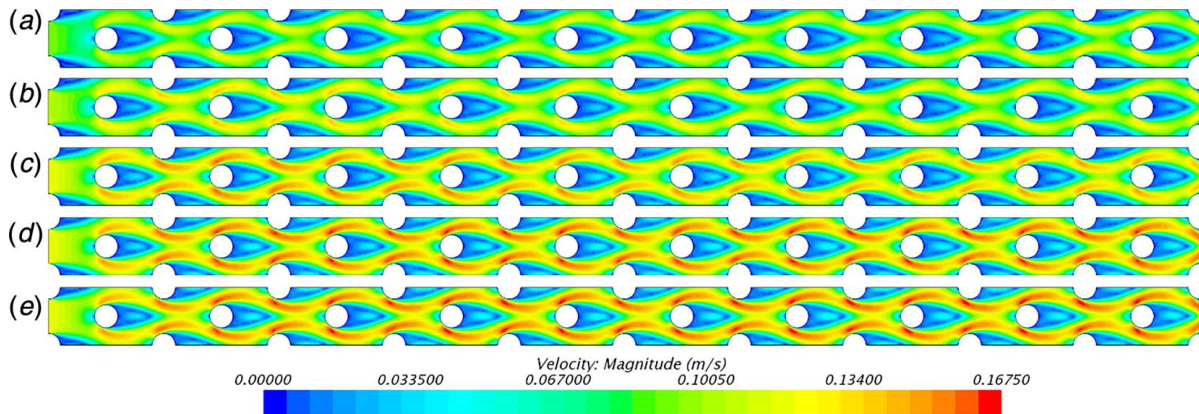


Fig. 9 Temporal evolution of the velocity field with 10-s ramp duration (on velocity) for air at $Re = 50$, $\varepsilon = 0.874$

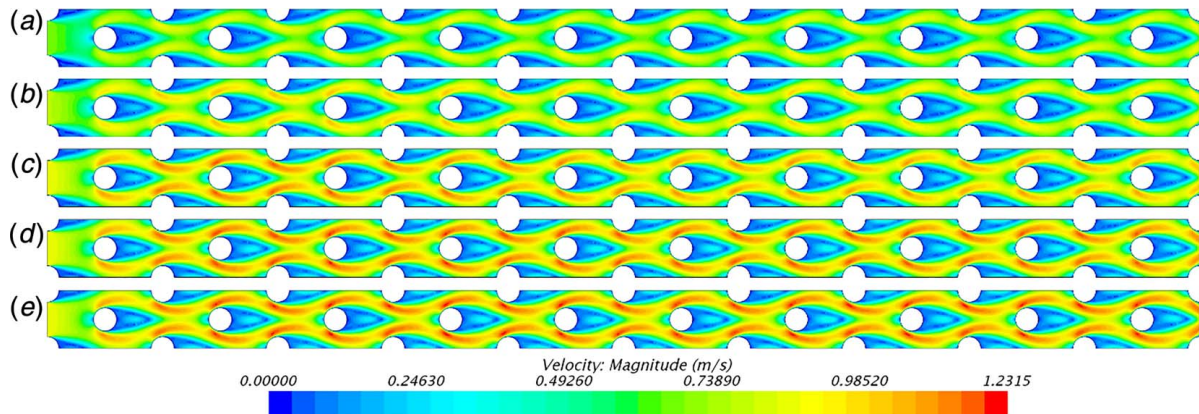


Fig. 10 Temporal evolution of the velocity field with 10-s ramp duration (on velocity) for H_2 at $Re = 250$, $\varepsilon = 0.874$

the thermal diffusion and viscous effects incurred around the obstacles when compared with air. This is observed in the response lag ratio of hydrogen in Fig. 11(a), where all respective porosities report a higher response lag ratio when compared with its counterpart, air. A monotonic increase in the response lag ratio is observed for air across all three porosities of the system. However, hydrogen exhibits a response lag ratio further downstream for larger porosities. The change in porosity amongst different working fluids is further analyzed in Fig. 11(b). The common trend changed where the largest porosity outputs a higher response lag ratio for

high-density fluids (carbon dioxide and air), and the opposite is noted for hydrogen when compared with the lowest porosity. As the Reynolds number is increased with decreasing porosity, the RLR decreases rather than increasing for air and carbon dioxide due to their fluid properties. With hydrogen being more sensitive and less dense, the change in the Reynolds number with porosity has little or no effect in the overall RLR.

The RLR is further discussed under the variable parameters of amplitude and ramp duration for the different working fluids. Figure 12(a) shows that the increase in amplitude augments the

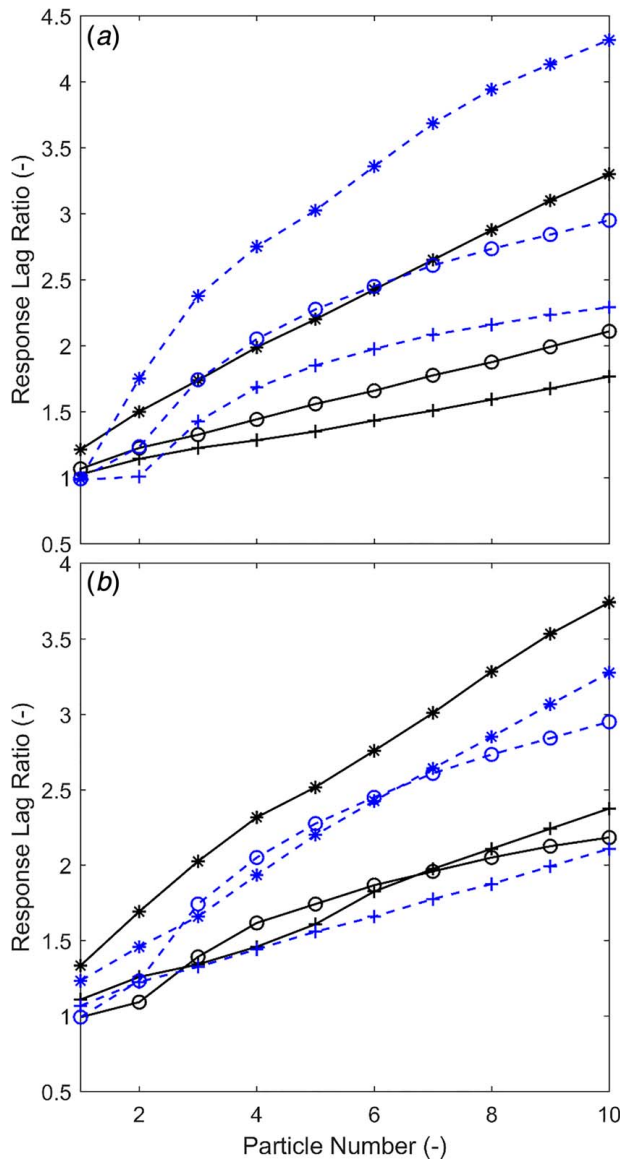


Fig. 11 (a) The RLR for air (black) and H2 (blue) at porosities of 0.87 (+), 0.80 (o) and 0.72 (*) when $Re = 250$. (b) The RLR for 0.87 (black, $Re = 150$) and 0.80 (blue, $Re = 250$) porosities and air (+), H2 (o) and CO2 (*). (Color version online.)

inlet velocity and therefore increasing forced convective heat transfer and viscous effects around the obstacles, resulting in a higher response lag ratio. Fluid properties continue to impact the degree of RLR reported, with hydrogen (lower density fluid) showcasing larger increases in RLR as the amplitude increases. However, for air (higher density fluid), although there is an increase in RLR, it is minimal. A general trend is also observed in Fig. 12(b), as the ramp duration is prolonged amongst the working fluid the RLR is noted to decrease. The lower RLR is reported as the gradual increase in velocity due to longer ramp duration decays the viscous effects and allows more time for heat to transfer from the circular obstacles to fluid with ease. Contrary to the previous trend reported in Fig. 12(a), Fig. 12(b) showcases higher RLR for air than hydrogen in general. Yet, it is also more responsive to the increase in ramp duration allowing the system to adapt to a higher density fluid resulting in a lower RLR than hydrogen for a 30-s ramp duration. The RLR being the response lag ratio is representative of the attenuation effect of the porous medium upon an input disturbance. Such attenuation is generally more intense when the disturbance includes strong gradients. For a ramp

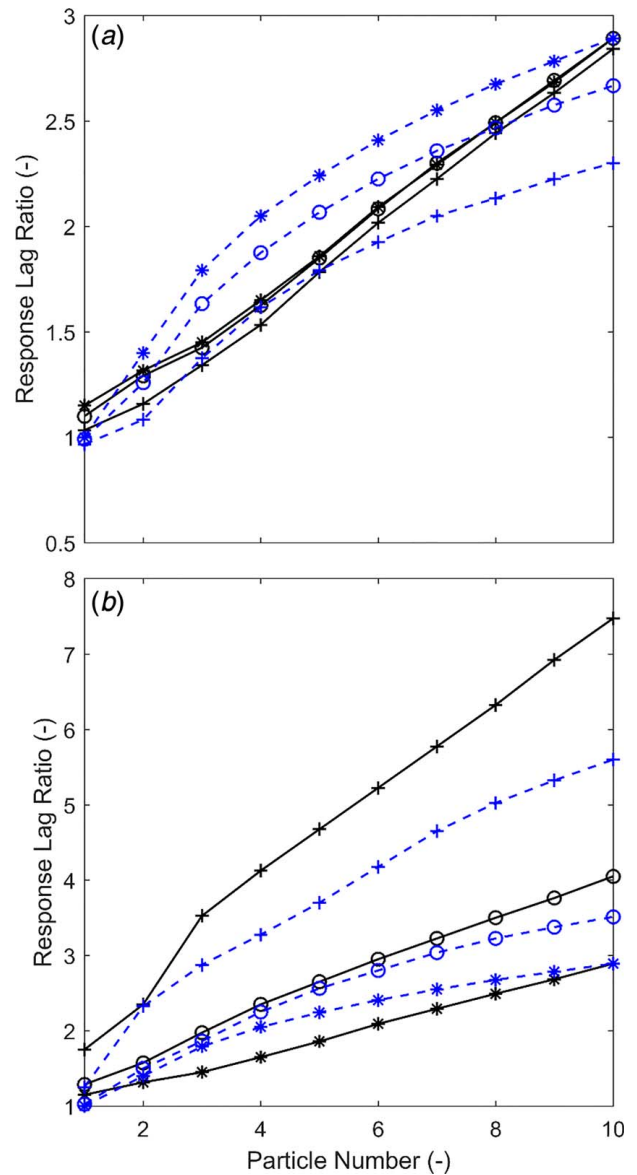


Fig. 12 (a) The effect of ramp amplitude on RLR for air (solid black) and H2 (dash blue) at 10% (+), 20% (o) and 30% (*) amplitudes during a 30 s ramp duration. (b) The effect of ramp duration on RLR for air (solid black) and H2 (dash blue) at 10 s (+), 20 s (o), and 30-s (*) durations for 30% amplitude. (Color version online.)

disturbance, strong gradients imply higher amplitude and shorter duration. That is why in Fig. 12 increase of Ramp amplitude results in higher values of RLR while increases in ramp duration reduces that.

4 Conclusions

A pore-scale analysis was conducted to study the effects of forced convection in porous media subject to a ramp disturbance superimposed on the entrance of a reticulated porous structure. Comprehending the transient response of porous media has grown in importance with its widespread use in numerous emerging applications. This study allows the prediction of thermal response of the pertinent system subject to time-dependent disturbances at the inlet. The porous model was made up of ten consecutive cylindrical obstacles with set isothermal boundary conditions and was subject to ramp disturbance for the flow velocity and temperature at the inlet. The RLR and transient behavior at each obstacle was

examined in detail by monitoring the spatiotemporal evolution of the flow and temperature fields as well as the surface-averaged Nusselt number.

Their key findings are as follows:

- An imposed ramp temperature disturbance at the inlet has an identical thermal response throughout the system, where an inlet velocity ramp input shows a varying response for each cylindrical obstacle. This makes a pore-scale analysis essential to monitor the transient thermal response of a porous structure.
- An increase in the Reynolds number has a minuscule rise on the RLR.
- An increase in porosity decreases the RLR. Yet, when the Reynolds number is decreased for a structure with a large porosity, RLR increases for high-density fluids only (air and carbon dioxide).
- An increase in the amplitude increases the RLR.
- An increase in the ramp duration decreases the RLR, more strongly for high-density fluids.

Acknowledgment

N. Karimi and B. Yadollahi acknowledge the financial support of Engineering and Physical Science Research Council (Grant No. EP/N020472/1).

Nomenclature

- a = amplitude = $\max \cdot u - \min \cdot u$
 k = thermal conductivity ($\text{W K}^{-1} \text{m}^{-1}$)
 p = pressure (Pa)
 t = time (s)
 u = flow velocity (m s^{-1})
 D = obstacle diameter (m)
 H = height (m)
 T = temperature (K)
 c_p = specific heat capacity ($\text{J K}^{-1} \text{kg}^{-1}$)
 h_o = external heat loss coefficient ($\text{W m}^{-2} \text{K}^{-1}$)
 q' = heat flux (W m^{-2})
 Nu = Nusselt number (–)
 Pr = Prandtl number (–)
 Re = Reynolds number (–)

Greek Symbols

- ε = porosity
 μ = dynamic viscosity ($\text{kg m}^{-1} \text{s}^{-1}$)
 ρ = density (kg m^{-3})
 ψ = temperature/velocity

Subscripts

- f = fluid
 in = inlet
 L = based on obstacle diameter size
 ramp = function of ramp
 ref = reference
 x, y, z = Cartesian coordinates

References

- [1] Cao, J., and Djilali, N., 2005, "Numerical Modeling of PEM Fuel Cells Under Partially Hydrated Membrane Conditions," *ASME J. Energy Resour. Technol.*, **127**(1), pp. 26–36.
- [2] Dokhani, V., Yu, M., Gao, C., and Bloys, J., 2018, "Investigating the Relation Between Sorption Tendency and Hydraulic Properties of Shale Formations," *ASME J. Energy Resour. Technol.*, **140**(1), p. 012902.
- [3] Movahedi, H., Vasheghani Farahani, M., and Masihi, M., 2020, "Development of a Numerical Model for Single- and Two-Phase Flow Simulation in Perforated Porous Media," *ASME J. Energy Resour. Technol.*, **142**(4), p. 042901.
- [4] Shahangian, N., Honnery, D., and Ghojel, J., 2014, "The Role of Porous Media in Homogenization of High Pressure Diesel Fuel Spray Combustion," *ASME J. Energy Resour. Technol.*, **136**(1), p. 012202.
- [5] Meng, X., and Yang, D., 2019, "Critical Review of Stabilized Nanoparticle Transport in Porous Media," *ASME J. Energy Resour. Technol.*, **141**(7), p. 070801.
- [6] Targui, N., and Kahalerras, H., 2013, "Analysis of a Double Pipe Heat Exchanger Performance by Use of Porous Baffles and Pulsating Flow," *Energy Convers. Manag.*, **76**, pp. 43–54.
- [7] Hunt, G., Torabi, M., Govone, L., Karimi, N., and Mehdizadeh, A., 2018, "Two-Dimensional Heat and Mass Transfer and Thermodynamic Analyses of Porous Microreactors With Soret and Thermal Radiation Effects—An Analytical Approach," *Chem. Eng. Process.—Process Intensif.*, **126**, pp. 190–205.
- [8] Hunt, G., Karimi, N., Yadollahi, B., and Torabi, M., 2019, "The Effects of Exothermic Catalytic Reactions Upon Combined Transport of Heat and Mass in Porous Microreactors," *Int. J. Heat Mass Transf.*, **134**, pp. 1227–1249.
- [9] Kolb, G., 2013, "Review: Microstructured Reactors for Distributed and Renewable Production of Fuels and Electrical Energy," *Chem. Eng. Process. Process Intensif.*, **65**, pp. 1–44.
- [10] Yuan, J., and Sundén, B., 2013, "On Continuum Models for Heat Transfer in Micro/Nano-Scale Porous Structures Relevant for Fuel Cells," *Int. J. Heat Mass Transf.*, **58**(1–2), pp. 441–456.
- [11] Wang, Y., Chen, K. S., Mishler, J., Cho, S. C., and Adroher, X. C., 2011, "A Review of Polymer Electrolyte Membrane Fuel Cells: Technology, Applications, and Needs on Fundamental Research," *Appl. Energy*, **88**(4), pp. 981–1007.
- [12] Deng, Y., Feng, C., Zhu, J. E. H., Chen, J., Wen, M., and Yin, H., 2018, "Effects of Different Coolants and Cooling Strategies on the Cooling Performance of the Power Lithium Ion Battery System: A Review," *Appl. Therm. Eng.*, **142**, pp. 10–29.
- [13] Xia, G., Cao, L., and Bi, G., 2017, "A Review on Battery Thermal Management in Electric Vehicle Application," *J. Power Sources*, **367**, pp. 90–105.
- [14] Wood, S., and Harris, A. T., 2008, "Porous Burners for Lean-Burn Applications," *Prog. Energy Combust. Sci.*, **34**(5), pp. 667–684.
- [15] He, F., and Ma, L., 2015, "Thermal Management of Batteries Employing Active Temperature Control and Reciprocating Cooling Flow," *Int. J. Heat Mass Transf.*, **83**, pp. 164–172.
- [16] Chu, X., Yang, G., Pandey, S., and Weigand, B., 2019, "Direct Numerical Simulation of Convective Heat Transfer in Porous Media," *Int. J. Heat Mass Transf.*, **133**, pp. 11–20.
- [17] Torabi, M., Peterson, G. P., Torabi, M., and Karimi, N., 2016, "A Thermodynamic Analysis of Forced Convection Through Porous Media Using Pore Scale Modeling," *Int. J. Heat Mass Transf.*, **99**, pp. 303–316.
- [18] Ozgumus, T., and Mobedi, M., 2014, "Effect of Pore to Throat Size Ratio on Interfacial Heat Transfer Coefficient of Porous Media," *ASME J. Heat Transf.*, **137**(1), p. 012602.
- [19] Mahmoudi, Y., and Karimi, N., 2014, "Numerical Investigation of Heat Transfer Enhancement in a Pipe Partially Filled With a Porous Material Under Local Thermal Non-equilibrium Condition," *Int. J. Heat Mass Transf.*, **68**, pp. 161–173.
- [20] Karimi, N., Agbo, D., Talat Khan, A., and Younger, P. L., 2015, "On the Effects of Exothermicity and Endothermicity Upon the Temperature Fields in a Partially-Filled Porous Channel," *Int. J. Therm. Sci.*, **96**, pp. 128–148.
- [21] Saito, M. B., and de Lemos, M. J. S., 2006, "A Correlation for Interfacial Heat Transfer Coefficient for Turbulent Flow Over an Array of Square Rods," *ASME J. Heat Transf.*, **128**(5), pp. 444–452.
- [22] Torabi, M., Karimi, N., Zhang, K., and Peterson, G. P., 2016, "Generation of Entropy and Forced Convection of Heat in a Conduit Partially Filled With Porous Media—Local Thermal non-Equilibrium and Exothermicity Effects," *Appl. Therm. Eng.*, **106**, pp. 518–536.
- [23] Hunt, G., Karimi, N., and Torabi, M., 2018, "Two-Dimensional Analytical Investigation of Coupled Heat and Mass Transfer and Entropy Generation in a Porous, Catalytic Microreactor," *Int. J. Heat Mass Transf.*, **119**, pp. 372–391.
- [24] Mahmoudi, Y., Hooman, K., and Vafai, K., 2019, *Convective Heat Transfer in Porous Media*, CRC Press, Boca Raton, FL.
- [25] Habib, R., Yadollahi, B., Karimi, N., and Hossein, M., 2020, "On the Unsteady Forced Convection in Porous Media Subject to Inlet Flow Disturbances—A Pore-Scale Analysis," *Int. Commun. Heat Mass Transf.*, **116**, p. 104639.
- [26] Saito, M. B., and de Lemos, M. J. S., 2005, "Interfacial Heat Transfer Coefficient for Non-equilibrium Convective Transport in Porous Media," *Int. Commun. Heat Mass Transf.*, **32**(5), pp. 666–676.
- [27] Kuwahara, F., Shirota, M., and Nakayama, A., 2001, "A Numerical Study of Interfacial Convective Heat Transfer Coefficient in Two-Energy Equation Model for Convection in Porous Media," *Int. J. Heat Mass Transf.*, **44**(6), pp. 1153–1159.
- [28] Lu, T., Jiang, P. X., Guo, Z. J., Zhang, Y. W., and Li, H., 2010, "Large-Eddy Simulations (LES) of Temperature Fluctuations in a Mixing Tee With/Without a Porous Medium," *Int. J. Heat Mass Transf.*, **53**(21–22), pp. 4458–4466.
- [29] Kim, S. Y., Kang, B. H., and Hyun, J. M., 1994, "Heat Transfer From Pulsating Flow in a Channel Filled With Porous Media," *Int. J. Heat Mass Transf.*, **37**(14), pp. 2025–2033.
- [30] Guo, Z., Kim, S. Y., and Sung, H. J., 1997, "Pulsating Flow and Heat Transfer in a Pipe Partially Filled With a Porous Medium," *Int. J. Heat Mass Transf.*, **40**(17), pp. 4209–4218.
- [31] Bhargava, R., Takhar, H. S., Rawat, S., Bég, T. A., and Bég, O. A., 2007, "Finite Element Solutions for Non-Newtonian Pulsatile Flow in a Non-Darcian Porous Medium Conduit," *Nonlinear Anal. Model. Control*, **12**(3), pp. 317–327.

- [32] Huang, P.-C., and Yang, C.-F., 2008, "Analysis of Pulsating Convection From Two Heat Sources Mounted With Porous Blocks," *Int. J. Heat Mass Transf.*, **51**(25–26), pp. 6294–6311.
- [33] Dhahri, H., Slimi, K., and Ben Nasrallah, S., 2008, "Entropy Generation for Pulsating Flow in a Composite Fluid/Porous System," *J. Porous Media*, **11**(6), pp. 557–574.
- [34] Forooghi, P., Abkar, M., and Saffar-Avval, M., 2011, "Steady and Unsteady Heat Transfer in a Channel Partially Filled With Porous Media Under Thermal Non-Equilibrium Condition," *Transp. Porous Media*, **86**(1), pp. 177–198.
- [35] Ghafarian, M., Mohebbi-Kalhari, D., and Sadeghi, J., 2013, "Analysis of Heat Transfer in Oscillating Flow Through a Channel Filled With Metal Foam Using Computational Fluid Dynamics," *Int. J. Therm. Sci.*, **66**, pp. 42–50.
- [36] Zaman, A., Ali, N., and Sajid, M., 2017, "Numerical Simulation of Pulsatile Flow of Blood in a Porous-Saturated Overlapping Stenosed Artery," *Math. Comput. Simul.*, **134**, pp. 1–16.
- [37] De Bortoli, A.L., Andreis, G. S. L., and Pereira, F. N., 2015, *Modeling and Simulation of Reactive Flows*, Elsevier, Burlington, MA, pp. 35–51.
- [38] Hunt, G., Karimi, N., and Torabi, M., 2017, "Analytical Investigation of Heat Transfer and Classical Entropy Generation in Microreactors—The Influences of Exothermicity and Asymmetry," *Appl. Therm. Eng.*, **119**, pp. 403–424.
- [39] Christodoulou, L., Karimi, N., Cammarano, A., Paul, M., and Navarro-Martinez, S., 2020, "State Prediction of an Entropy Wave Advecting Through a Turbulent Channel Flow," *J. Fluid Mech.*, **882**, p. A8.
- [40] Stone, H. A., and Duprat, C., 2016, *Fluid-Structure Interactions in Low-Reynolds-Number Flows*, Vol. 4, Royal Society of Chemistry, pp. 25–77.
- [41] Gamrat, G., Favre-Marinet, M., and Le Person, S., 2008, "Numerical Study of Heat Transfer Over Banks of Rods in Small Reynolds Number Cross-Flow," *Int. J. Heat Mass Transf.*, **51**(3–4), pp. 853–864.
- [42] Habib, R., Karimi, N., Yadollahi, B., Hossein, M., and Li, L. K. B., 2020, "A Pore-Scale Assessment of the Dynamic Response of Forced Convection in Porous Media to Inlet Flow Modulations," *Int. J. Heat Mass Transf.*, **153**, p. 119657.
- [43] Chen, C. J., and Wung, T.-S., 1989, "Finite Analytic Solution of Convective Heat Transfer for Tube Arrays in Crossflow: Part II—Heat Transfer Analysis," *ASME J. Heat Transf.*, **111**(3), pp. 641–648.